<u>Supplementary material to *Geophysical Research Letters* manuscript 2019GL083035</u>

"A 5.3-million-year history of monsoonal precipitation in northwestern Australia"

Jan-Berend W. Stuut[1,2,3], Patrick De Deckker[4], Mariem Saavedra-Pellitero[5], Franck Bassinot[6], Anna-Joy Drury[2], Maureen H. Walczak[4], Kana Nagashima[7], Masafumi Murayama[8]

[1]NIOZ – Royal Netherlands Institute for Sea Research, and Utrecht University, Texel, the Netherlands
[2]MARUM – Center for Marine Environmental Sciences, Bremen University, Bremen, Germany
[3]Department of Earth Sciences, Faculty of Science, Vrije Universiteit Amsterdam, The Netherlands
[4]ANU – Australian National University, Research School of Earth Sciences, Canberra, Australia
[5]Bremen University, Department of Geosciences, Bremen, Germany
[6]LSCE - Laboratoire des Sciences du Climate et de l'Environnement, Gif-sur-Yvette, France
[7]JAMSTEC – Japan Agency for Marine Earth Science and Technology, Yokosuka, Japan
[8]Center for Advanced Marine Core Research, Kochi University, Kochi, Japan

Selection of core sites

The detailed bathymetric map depicted in Figure S1 shows the exact core locations of the two studied cores ODP122-762B and MD002316. These core sites were selected on the basis of bathymetric mapping and seismic profiling carried out in 1988 and 2000, respectively. The core sites were chosen such that they are not prone to contain the results of mass wasting such as slope failure or turbidite deposits. Core ODP122-762B was drilled on the top of the Montebello Saddle, which forms a large plateau on the northwestern Australian continental slope [*Haq et al.*, 1990]. Core MD002361 was retrieved from a saddle in between the Cape Range Canyon and the Cloates Canyon, to avoid mass deposits that may have flown through these canyons [*Spooner et al.*, 2011].

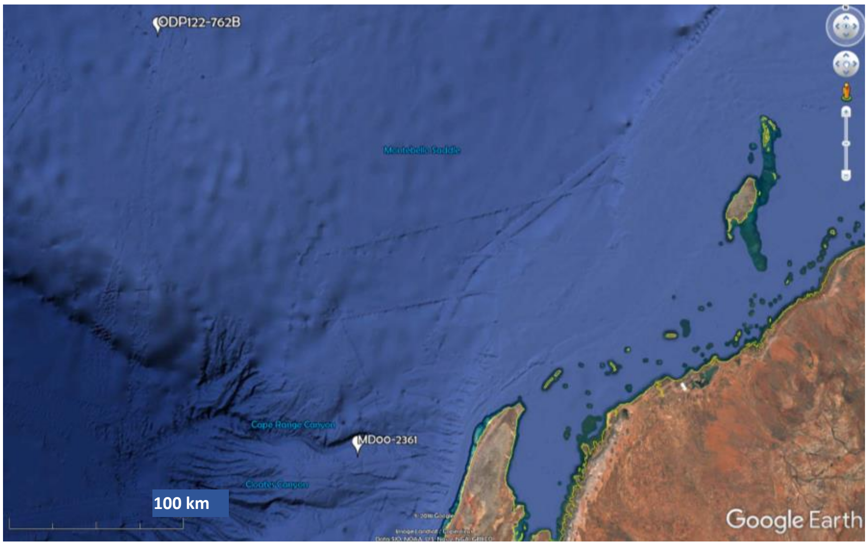

Figure S1. Detailed bathymetric map of the northwestern Australian continental slope with the exact positions of the core sites ODP122-762B and MD00-2361. Straight lines on the map show locations of detailed bathymetric mapping.

The two sediment cores were checked carefully for any signs of mass wasting which had not been found by Stuut et al., [2014] in the upper half of the core (<550 ka). A disturbance was found at the bottom of core MD002361, and which was dated at about 1 Ma. This timing coincides with a large mass-wasting event that is well-known in the area and which was observed in numerous sediment records (Dr S. Gallagher, *pers. com*.). For this reason, we did not present the part of sediment core MD002361 older than 1 Myr. For sediment core ODP122-762B, no turbidite sequence has been observed by the sedimentologists on board *RV Joides Resolution [Haq et al., 1990]*, by us, nor in the papers by Tang [1992], nor in Wells and Chivas [1994]. The absence of this event in core ODP122-762B at about 1 Myr most likely is related to the fact that also this core was drilled from a ridge that stands above channels through which a turbidite was most likely funnelled into the Indian Ocean or it is simply too distal for this event to have reached it. Further confirmation for continuous sedimentation stems from the uninterrupted $\delta^{18}O$ chronologies of both cores as well as the excellent correspondence in the bulk-chemical records between them.

Relationship between present-day precipitation and ENSO

Presently, the monsoonal climate of northern Australia is strongly influenced by the El Niño Southern Oscillation (ENSO), which is related to the Southern Oscillation Index (SOI). The SOI is a standardized index based on the observed sea-level pressure differences between the central-Pacific island of Tahiti and Darwin, Australia. These pressure differences reflect the east-west sea-surface temperature and air-pressure gradients typical for El Niño and La Niña episodes. A negative phase of the SOI represents below-average air pressure at Tahiti and above-average air pressure at Darwin. Prolonged periods of negative SOI values coincide with anomalously warm ocean waters across the eastern tropical Pacific, which are typical of El Niño episodes. The opposite holds for La Niña situations.

Typically, tropical-cyclone (TC) activity is increased during so-called neutral years and La Niña years [*Dare*, 2013]. Present-day observations confirm this relationship between the SOI, TC-related rainfall in northern West Australia, and river runoff [*Dare et al.*, 2012]. This relationship is illustrated by comparing the SOI with precipitation in the TC months (November – March) at three monitoring stations at airports in northwestern Australia and river runoff of three rivers draining into the eastern Indian Ocean: the Gascoyne River, Lyndon River and Ashburton River (figs.S2A and S2D). The general relationship is that during periods of positive SOI, rainfall and river runoff are increased. Rivers in northwestern Australia remain dry during most of the year and carry vast loads of suspended sediments during sparse flooding events (see fig.S2B: Gascoyne River at Nine-mile bridge during flooding event in 2010 and fig.S2C: the Gascoyne River spilling huge amounts of sediments into the eastern Indian Ocean during the flooding event following TC Kelvin in March 2018). These large amounts of sediments are eventually deposited on the ocean floor of the northwestern Australian continental margin via the shallow Ningaloo *(counter)* Current (fig.1) and can be reconstructed on the basis of bulk chemistry and particle size of the terrigenous fraction. As a result, we interpret the observed changes in sediment composition in the two studied sediment cores in terms of fluvial-mud transport, ultimately related to monsoonal rainfall in northwestern Australia.

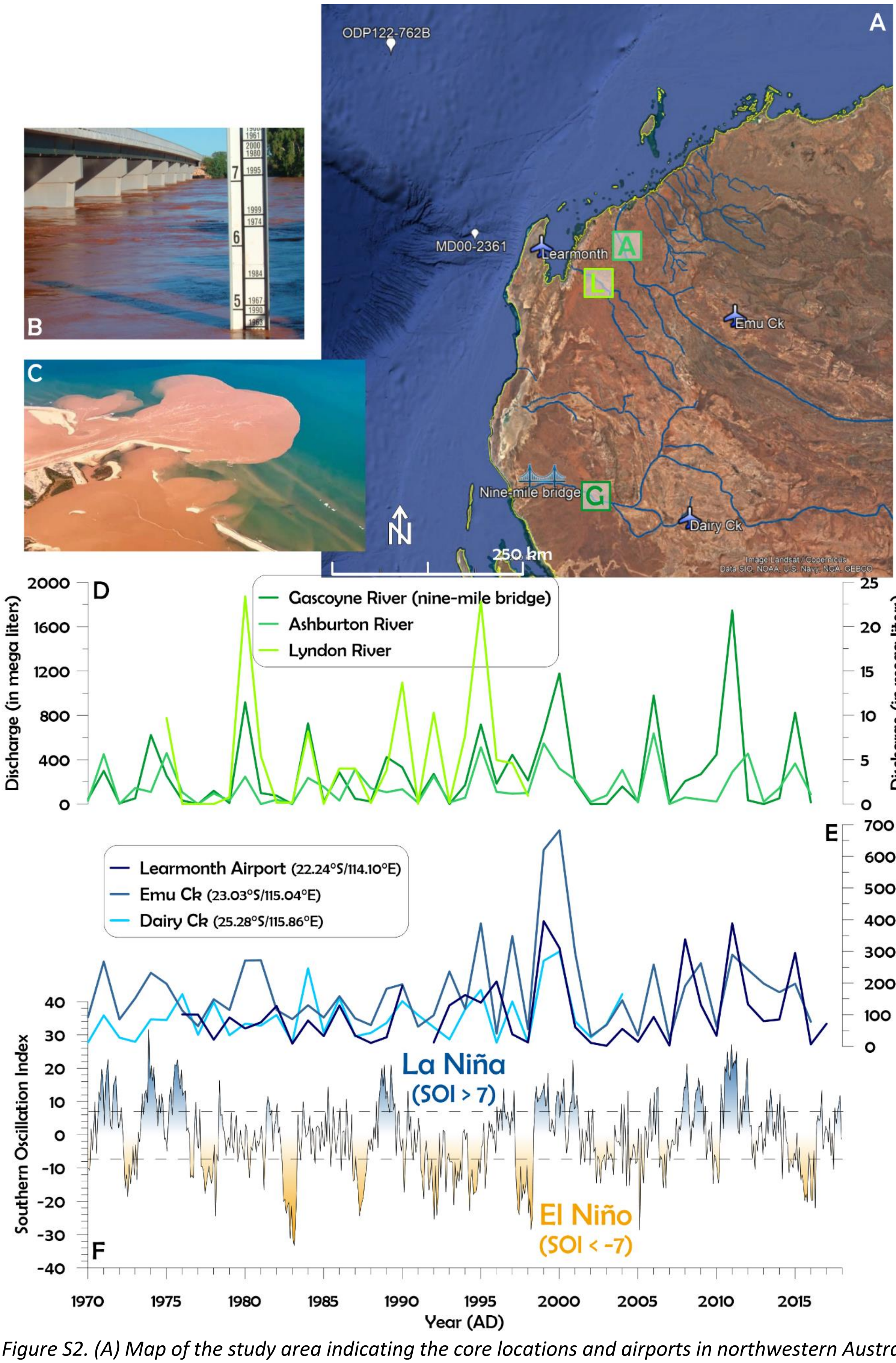

Figure S2. (A) Map of the study area indicating the core locations and airports in northwestern Australia where rainfall is being recorded as well the major rivers of which discharges have been plotted in figure D: G = Gascoyne River, recorded at nine-mile bridge, A = Ashburton River, L = Lyndon River. (B) photo of the Gascoyne River at nine-mile bridge during a flooding event in 2010 (from: <u>*double-*</u>

barreledtravel.com/the-gascoyne-river-comes-to-life) (C) the sediment load of the Gascoyne River spilling into the eastern Indian Ocean at Carnarvon after Tropical Cyclone Kevin in March 2018 (picture by Ryan John, from: www.perthnow.com.au/news/regional/was-gascoyne-river-flows-again-after-record-rain-ng-b887181z) (D) Discharge of three rivers draining into the study area: Lyndon River (much lower discharge, plotted on right y-axis, data until 1999), the Ashburton River, and the Gascoyne River measured at nine-mile bridge (E) TC-season (November – March) rainfall records recorded at the airports of Learmonth, Emu Creek and Dairy Creek, and (F), SOI. Data for records in D,E, and F were downloaded from the Australian Bureau of Meteorology website: www.bom.gov.au.

Dispersal of fluvial sediments in the deep sea

Although the distal core ODP122-762B is located on the northwestern continental shelf of Western Australia, about 330 km from the nearest coast, we claim that it directly registers the supply of fluvial sediments from rivers that drain the Western Australian hinterland. In a recent review of global sediment plumes by Shanmugam [2018], it was shown how suspended river sediments are dispersed both at the ocean's surface as well as along density layers of a large number of so-called hyperpycnal flows. In addition, just to name a few; River Nile floods were registered in the Mediterranean Sea at >200 km from the river mouth [*Ducassou et al.*, 2008], Congo River signatures were found in the Atlantic Ocean at >1000 km [*Hopkins et al.*, 2013; *Palma and Matano*, 2017], and Chinese river signatures were found in the South China Sea at >400 km from their estuary [*Kang et al.*, 2013]. In addition, the approach that we have taken is very similar to studies in the Indian Ocean [*Prins et al.*, 2000], in the southeast Atlantic Ocean [*Stuut et al.*, 2002], and in the southeast Pacific Ocean [*Stuut and Lamy*, 2004; *Stuut et al.*, 2007]. These studies all conclude that the proportion of fluvial mud increases with distance to the coast and that fluvial sediments are still clearly recognised up to 670 km from the river mouth, sedimentation rates are similar to the ones observed in our study.

Moreover, it was shown in sediment cores located at large distances from the Australian mainland (up to 600 km, see fig.S3-D) that alternating fluvial and aeolian sedimentation can be clearly distinguished during the past 25kyr on the basis of the same XRF-scanning technique that we apply [*Kuhnt et al.*, 2015]. These cores are located at large distances (up to 600 km, see fig.S3-D) from the Australian mainland.

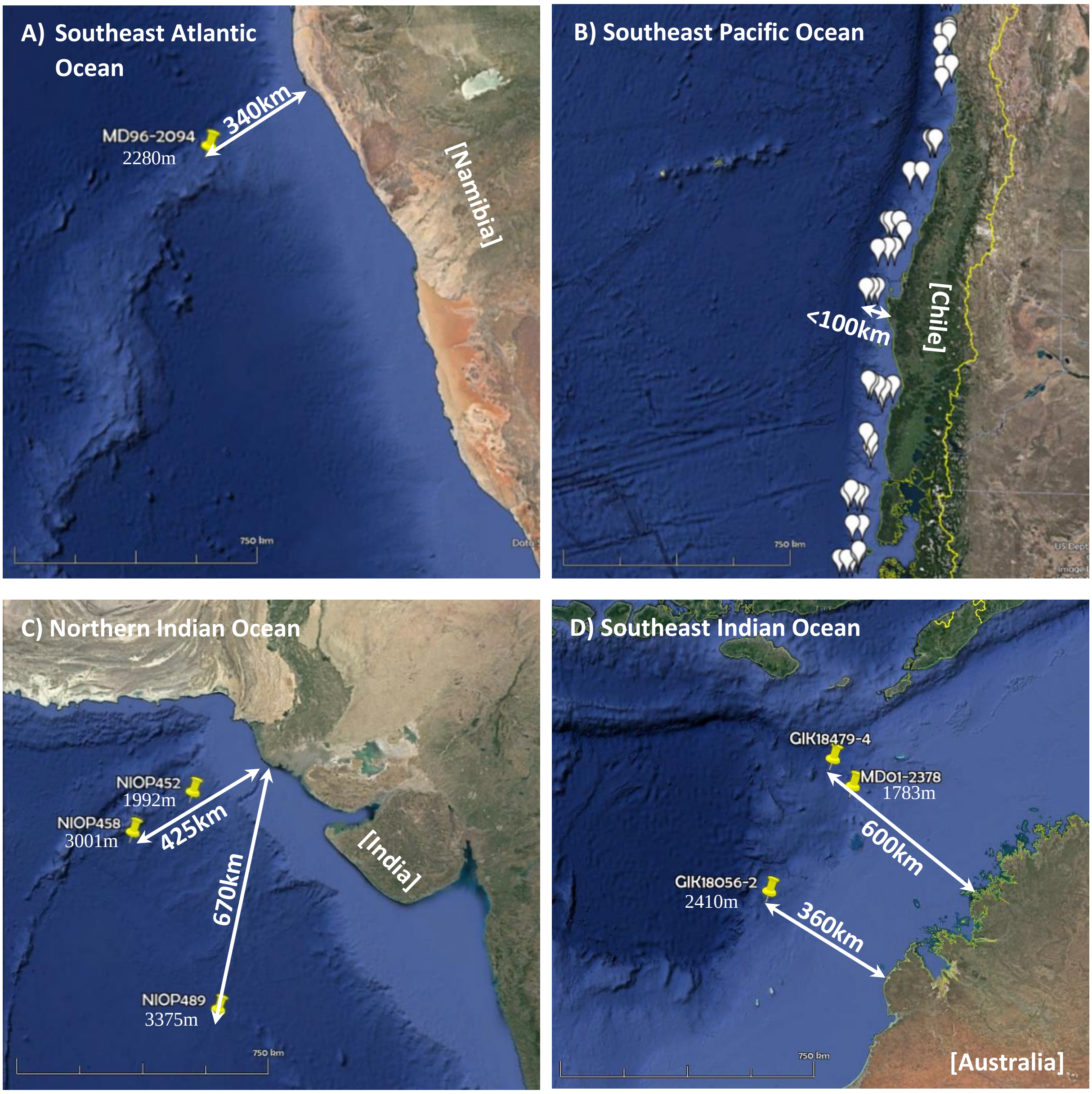

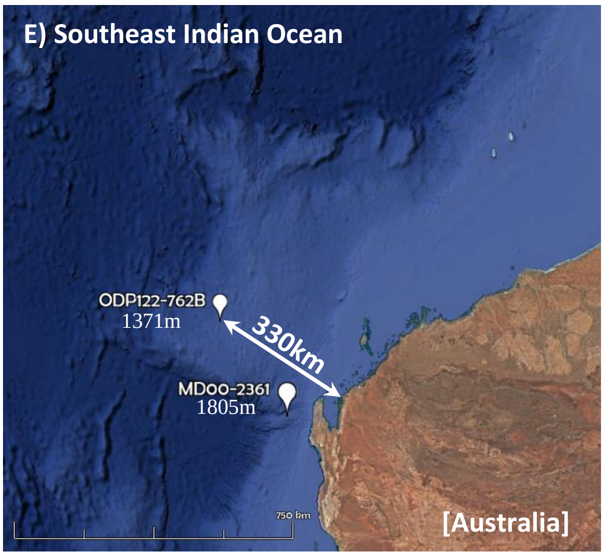

Figure S3. Google Earth maps of the core sites of four studies (*A [Stuut et al., 2002], B [Stuut and Lamy, 2004; Stuut et al., 2007], C [Prins et al., 2000], D [Kuhnt et al., 2015]*) compared with the Australian study area discussed in this paper (E). All studies distinguish between fluvial and aeolian sediments, recognising that the proportion fluvial sediments increases relative to aeolian with distance to the coast. The scale bar in each panel is 750 km. Arrows in figures A and B show distance to the nearest shore, which is actually much smaller than the actual distance to the river mouth.

Proxy records from bulk chemistry (XRF) and particle size

The combined evaluation of the bulk chemical analyses and particle size of the terrigenous fraction, published by Stuut et al., [2014] shows how the sediments of the upper part (last 500 ka) of sediment core MD00-2361 consist primarily of fluvial mud and wind-blown dust. The most evident proxies presented by Stuut et al., [2014] are summarised here (fig S4) and these results were extended for the MD00-2361 core down to 1 Ma in this paper.

Core MD00-2361 has a total length of 42m, of which the upper 22m cover the last 1 Ma (based on oxygen-isotope stratigraphy). At 23m core depth signs of mass wasting were observed, which may be related to a large turbidite that was found in many cores in the region at ~1 Ma (pers. Comm. Prof. S. Gallagher).

The two bulk-chemical proxies measured using an XRF core scanner (Log(Si/Al) and Log(Zr/Fe), see fig.S4) show how glacial- and interglacial stages are markedly different in sediment composition. Glacial stages are characterised by high Si and Zr values, which we interpret as typical aeolian origin. The interglacial stages are characterised by high Al and Fe values, which we interpret as typical fluvial origin. Based on an end-member approach applied to particle-size distributions of the terrigenous sediment fraction, Stuut et al., [2014] showed how at this proximal core site, the aeolian sediment fraction is distinctly coarser grained than the fluvial sediment fraction. Thus, for each sample the proportion aeolian dust and fluvial mud could be expressed, and which was interpreted as a proxy for continental humidity. The resulting downcore humidity record corroborates the bulk chemical records with a clear dominance of fluvial sediments during interglacial stages, as opposed to a dominance of aeolian sediments during glacial stages (fig. S5).

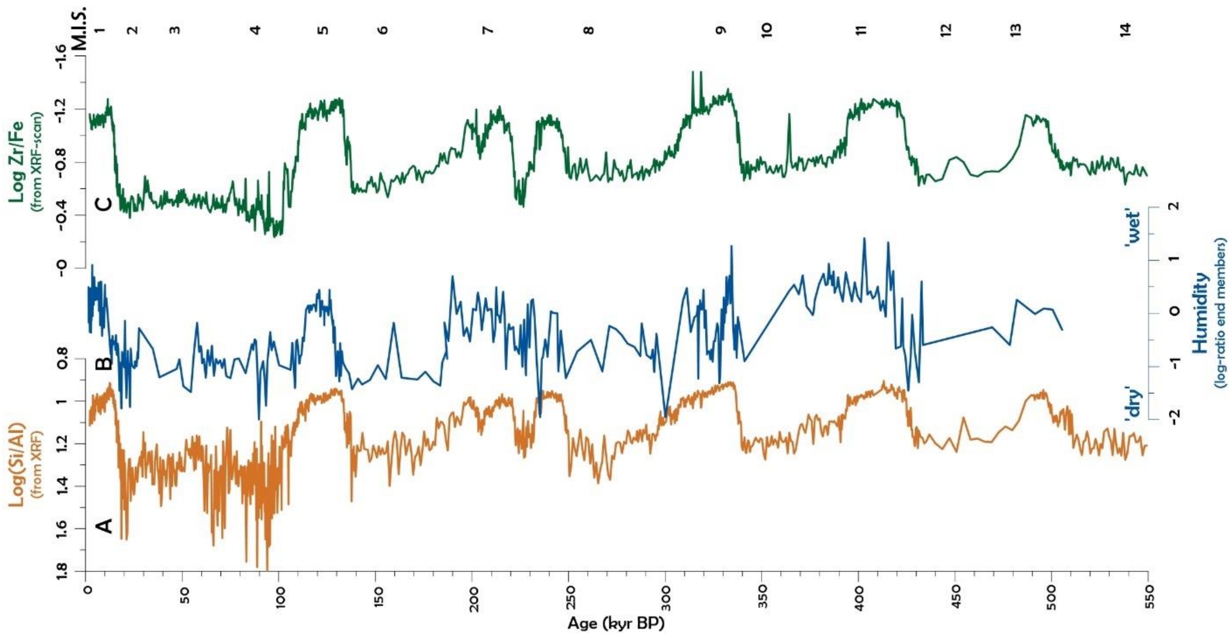

Figure S4. Most evident proxy records for northwestern Australian climate of the last 550 Ka (from core MD00-2361 and previously published by Stuut et al., [2014]. A) Log Si/Al, a proxy for different types of terrigenous sediment supply in which the Si is predominantly present in wind-blown dust as opposed to Al which is in the fine-grained fluvial mud; B) Continental humidity, expressed as a log-ratio of the fluvial and aeolian end members in the particle-size distributions of the terrigenous sediment fraction; C) Log Zr/Fe, a proxy for continental humidity with the Zr in the wind-blown sediment fraction and the Fe in the fluvial mud. MIS: Marine Isotopic Stages.

Linear sedimentation rates

Supporting evidence for the interpretation of our bulk-chemical and particle-size data follows from the linear sedimentation rates calculated by interpolating the amounts of sediment deposited per thousand years between the tie points of the age models of the two cores. Interglacial stages, which are dominated by fluvial sediments, ultimately related to intensive monsoonal activity, clearly show a pronounced higher amount of sediments deposited at the two sites as opposed to glacial stages, which consist mostly of marine carbonates and wind-blown coarse-grained quartz.

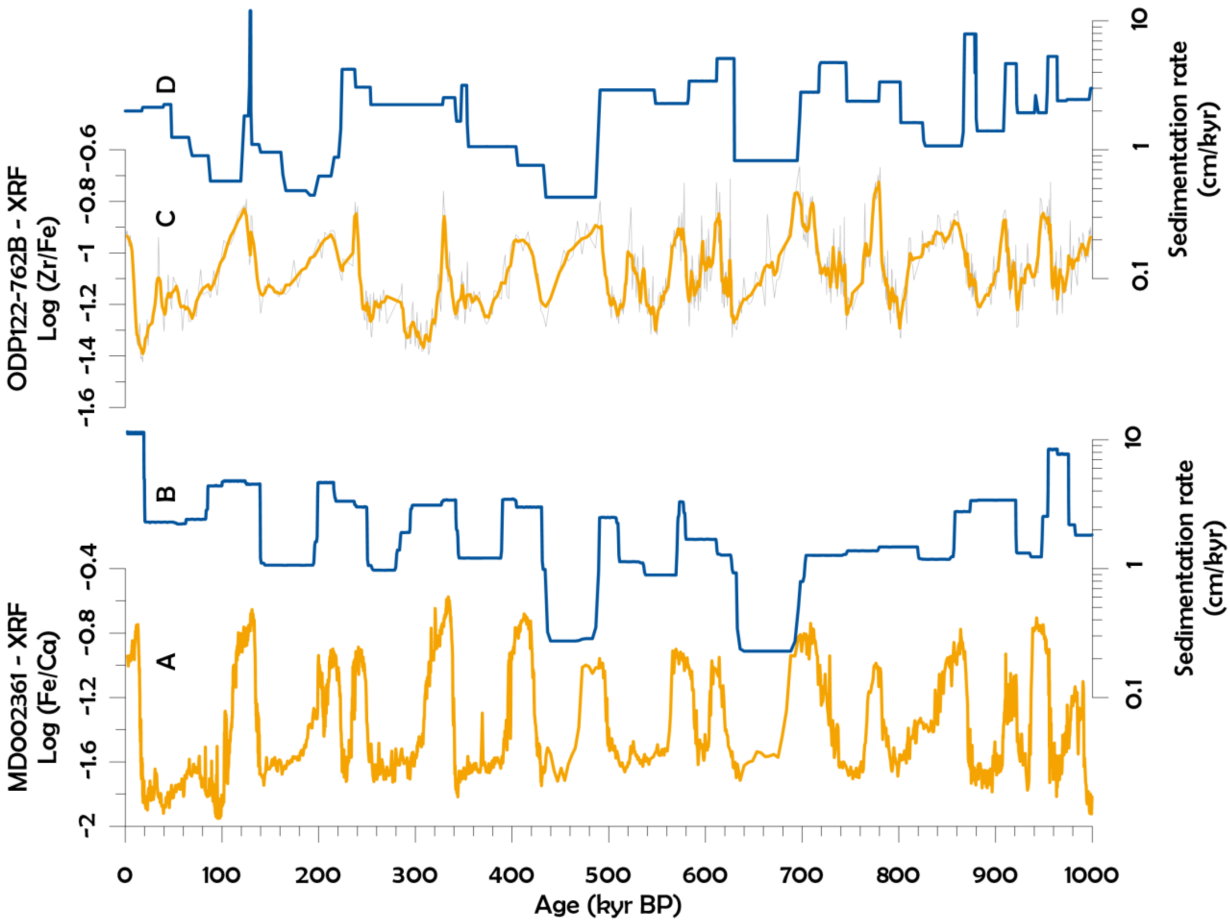

Figure S5. Proxy records for northwestern Australian climate of the last 1 Ma. A) MD00-2361 Log Fe/Ca, a proxy for terrigenous-sediment input [Stuut et al., 2014]. The lower 450 ka of the MD00-2361 records are new data, complementary to Stuut et al., [2014] B) MD00-2361 linear sedimentation rates as calculated from the age model showing high sedimentation rates during interglacial stages relative to glacial stages; C) ODP122-762B Log Fe/Ca raw data in grey, 5-point running average in orange; D) ODP122-762B linear sedimentation rates as calculated from the age model showing generally higher sedimentation rates during interglacial stages relative to glacial ones.

Measurements of bulk chemistry using XRF scans

Two different analysis types were used to obtain bulk-chemical records. The XRF records of core ODP122-762B were obtained using the Itrax XRF core scanner at Kochi Core Center, Japan. Elemental compositions of the elements Mg, Al, Si, P, S, Cl, Ar, K, Ca, Sc, Ti, V, Cr, Mn, Fe, Co, Ni, Cu, Zn, Ga, Br, Rb, Sr, Y, Zr, Ba, Ta, W, Os, Ir, Pt, and Pb were measured as counts per second. Due to the condition of the core sections, which were recovered from the ocean floor in 1988, only the heavier elements K to Zr gave reproducible measurements. Bulk chemical measurements of core MD002361 were obtained using the Avaatech XRF core scanner at NIOZ, the Netherlands. Elemental compositions of the elements Al, Si, S, Cl, K, Ca, Ti, Cr, Mn, Fe, Ni, Cu, Zn, Br, Rb, Sr, Y, Zr, and Pb were measured as counts per second. To avoid the problem of closed-sum [*Weltje and Tjallingii*, 2008], only Log-ratios of elements were used of Fe and Ca, representative of terrigenous and marine sediments, respectively. The Log(Fe/Ca) is therefore used as a proxy for land-derived material (see also the brown-coloured suspended sediments in the Gascoyne River in figs.S2B and S2C), in this case dominated by fluvial sediments supplied by the suite of rivers draining northwestern West Australia (fig.S2A).

In addition, zooming in on the terrigenous sediment fraction, we interpret the Log(Zr/Fe) as a proxy for wind-blown dust, also following Stuut et al., [2014]. In addition to these two proxies, we also investigated the Log(Si/Al) as a proxy for aeolian dust, knowing that the wind-blown material is dominated by quartz and the river-flown material is fine-grained and rich in aluminium [*Stuut et al.*, 2014]. To test the hypothesis that the aeolian and fluvial end members have distinctly different chemical compositions, we sampled dune systems and river beds in northwestern Western Australia (figs.1 and S6) and measured their bulk chemical composition using the Avaatech XRF scanner at NIOZ, using the same settings at which core MD00-2361 was measured.

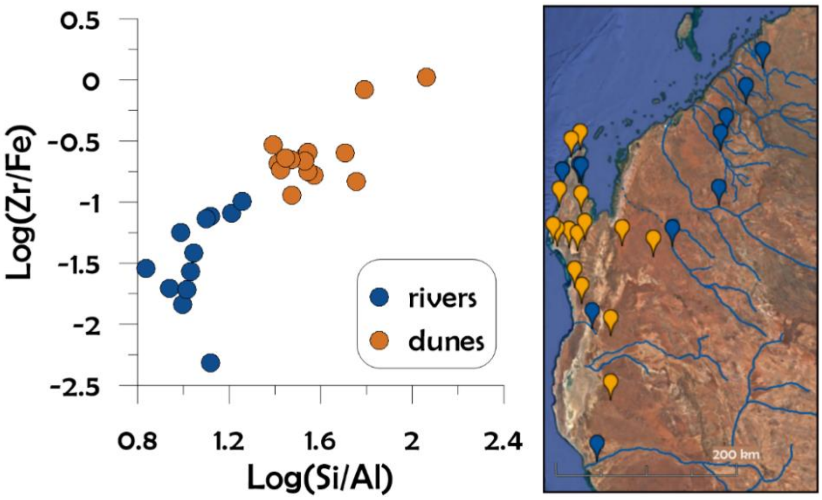

Figure S6. Bulk chemical composition of discrete samples from river beds and dune sediments in northwestern Western Australia. Cross plot of Log(Zr/Fe) and Log(Si/Al) shows how the two different types of sediment make up end-member compositions. These same bulk chemical ratios were plotted for the sediment core MD00-2361 in fig.S4, which further corroborate our interpretation of the proxy records.

The results show a distinct grouping of samples and a clear separation between the river samples and the dune samples with higher values for both Log(Si/Al) and Log(Zr/Fe) for the dune samples as opposed to the river samples. This separation into fluvial and aeolian end-members corroborates the bulk-chemical downcore results which show the same end-member separation throughout the last 1Ma (fig.S4). In addition, the data support the end-member approach based on the particle size with coarser-grained wind-blown sediments as opposed to finer-grained fluvial sediments.

Age model core ODP122-762B

The age model was based originally on the existing shipboard Magnetostratigraphy [*Tang*, 1992]. However, new calcareous nannofossil datum events [*Anthonissen and Ogg*, 2012], resulted in 16 new tie points (Table S1), which were assumed to be more precise than the preliminary shipboard data.

In total, thirty-one smear slides were prepared and analyzed for calcareous nannofossils, from 4 m to 101,75 m in the same Leica DMRM polarized light microscope at 1000x. The samples were taken every ca. 3 m. Therefore, there could be certain uncertainty in the biostratigraphic datums. Being conservative and assuming an average sedimentation rate of 1.88 cm/kyr for this sedimentary sequence (calculated from the ODP122-762B-tiepoints-L&R05 list) and our sampling interval of ca. 3 m, the maximum shift in ages would be of ca. 0.17Ma. However, the succession of calcareous nannofossil markers at ODP122-762B was clear and we are confident on the first and last occurrences observed and considered for this work.

Subsequently, a visual correlation of the Log(Fe/Ca) XRF record and the Lisiecki and Raymo [2005] stack was made, which resulted in 175 additional tie points (fig S7).

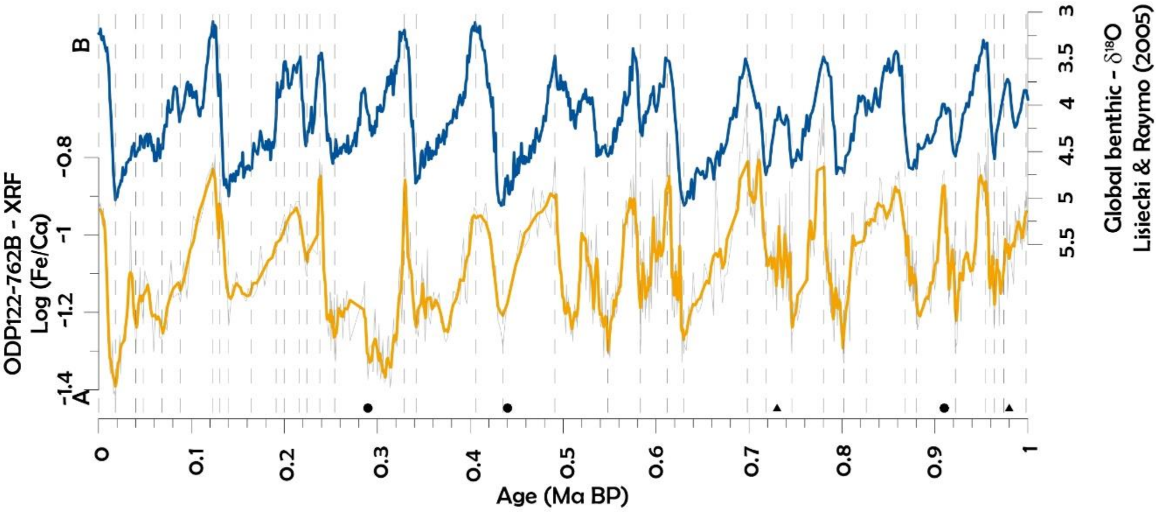

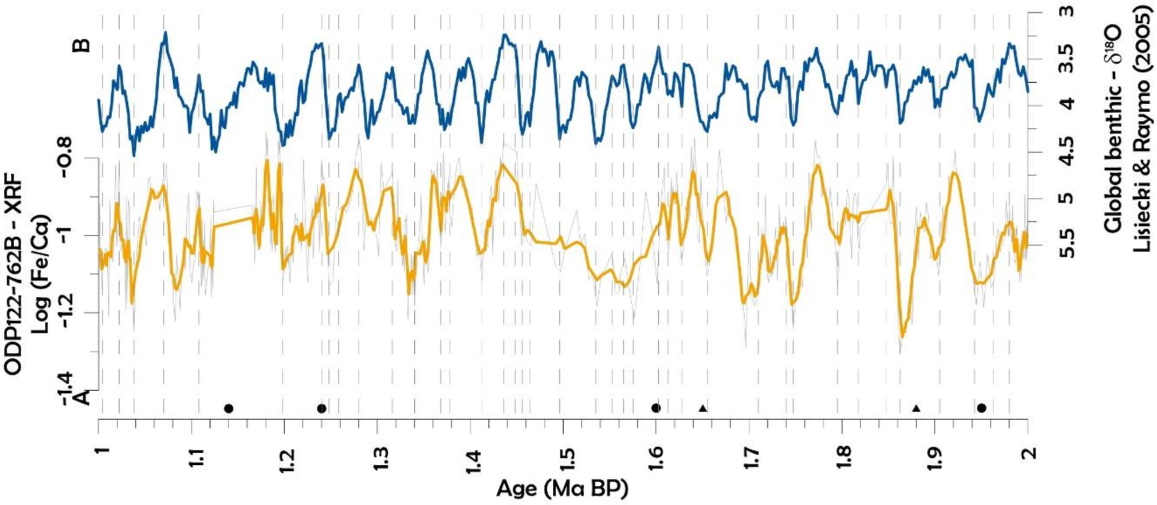

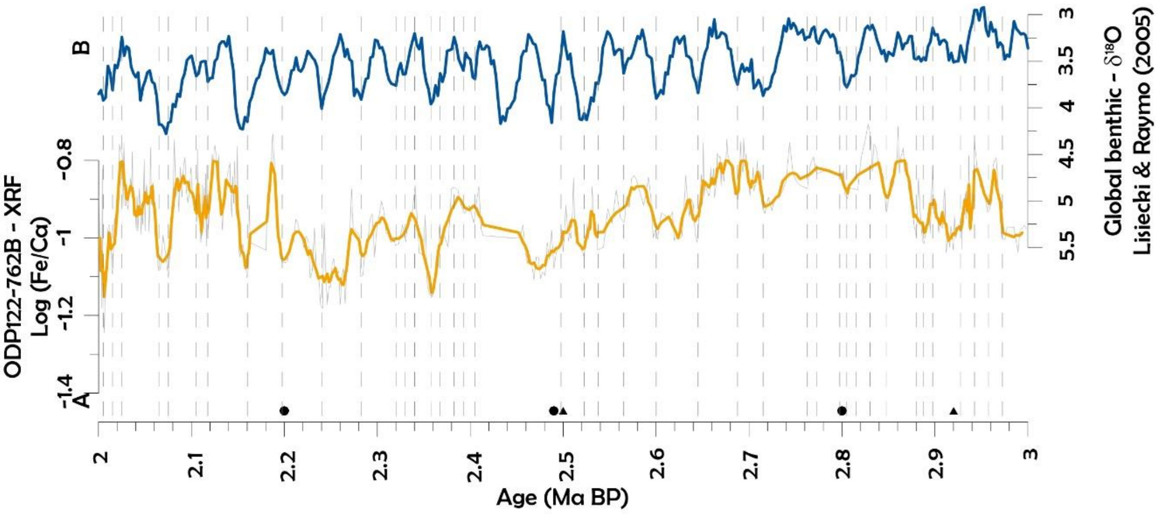

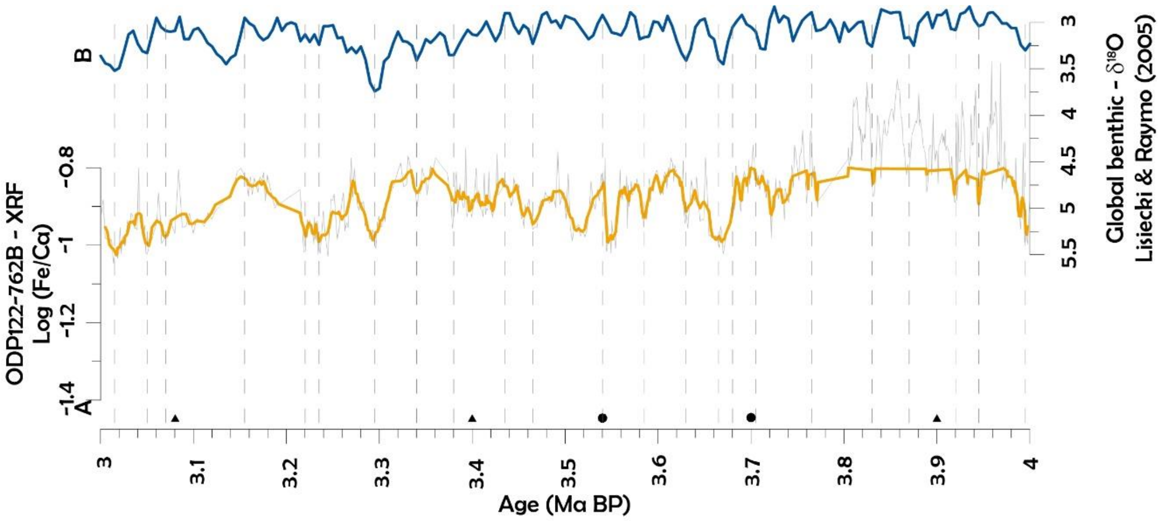

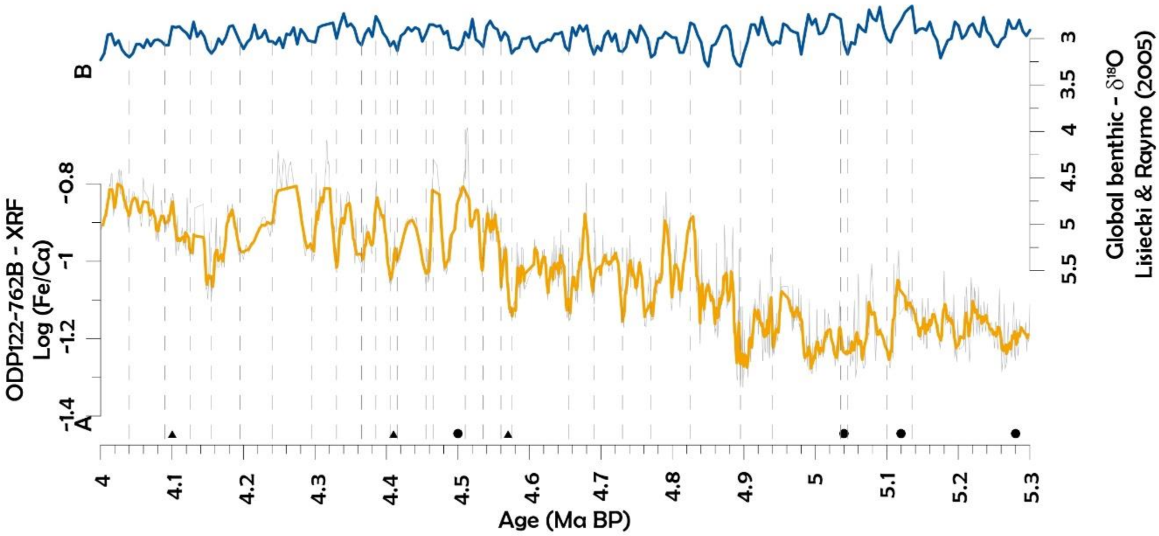

Figure S7. Plots showing the tie-points of the visual correlation of the Log(Fe/Ca) record to the Lisiecki & Raymo [2005] benthic stack. Also, the original magnetostratigraphic tie points by Tang [1992; black dots, N=16] and the new biostratigraphic tie points [black triangles, N=13] are shown.

Table S1. Biostratigraphic tie points obtained in this study based on calcareous nannofossil analyses compared with shipboard magnetostratigraphic tie points [Tang, 1992] on which the initial age model was based (FO: first occurrence, LO: last occurrence). Revised tie points of original shipboard Magnetostratigraphy are shown in grey.

Biostratigraphic Datum	Depth (mbsf)	Age (Ma)	Magnetostratigraphic Marker	Depth (mbsf)	Age (Ma)
FO *Emiliania huxleyi*	4	0.29	**Brunhes/Matuyama**	11.20	0.73
LO *Pseudoemiliania lacunosa*	7	0.44	**upper Jaramillo**	12.10	0.91
LO *Reticulofenestra asanoi* (common)	16.25	0.91	**lower Jaramillo**	13.10	0.98
FO *R. asanoi* (common)	22.75	1.14	**upper Olduvai**	25.00	1.65
LO Large *Gephyrocapsa* (>5.5 µm)	25.75	1.24	**lower Olduvai**	27.50	1.88
LO *Calcidiscus macintyrei*	29	1.6	**Matuyama/Gauss**	37.60	2.50
LO *Discaoaster triradiatus*	32.25	1.95	**Kaena**	47.20	2.92
FO *D. triradiatus* (acme)	38.5	2.2	**Mammoth**	51.40	3.08
LO *Discoaster surculus*	41.75	2.49	**Gauss/Gilbert**	62.10	3.40

LO *Discoaster tamalis*	44.75	2.8	**Cochiti**	71.60	3.90
LO *Sphenolithus* spp.	54.25	3.54	**Nunivak**	79.50	4.10
LO *Reticulofenestra pseudoumbilicus*	57.5	3.7	**Sidufjall**	84.50	4.41
LO *Amaurolithus primus*	73.25	4.5	**Thvera**	90.00	4.57
LO *Ceratolithus acutus*	89.25	5.04			
FO *Ceratolithus rugosus*	95.5	5.12			
LO *Triquetrorhabdulus rugosus*	101.25	5.28			

The samples were taken every ca. 3 m. Therefore, there could be certain uncertainty in the biostratigraphic datums. Being conservative and assuming an average sedimentation rate of 1.88 cm/kyr for this sedimentary sequence (calculated from the ODP122-762B-tiepoints-L&R05 list) and our sampling interval of ca. 3 m, the maximum shift in ages would be of ca. 0.17Ma. However, the succession of calcareous nannofossil markers at ODP122-762B was clear and we are confident on the first and last occurrences observed and considered for this work.

Time-series analysis

Power spectra were generated for the 5.3 Ma XRF records using the updated [*Grinsted et al.*, 2004] method of Torrence and Compo [1998], after detrending the data using a notch filter (removal of >1 Ma trend) and correcting for low-frequency wavelet bias following Liu et al., [2007]. In general, the detrended XRF wavelets show a stronger 40 ka beat at ~3 – 2.5 Ma and then a strong 95/125 Ka beat appearing just after 1 Ma, which is the well-known transition from the obliquity-dominated world to the eccentricity-dominated world at the mid-Pleistocene transition [*Lisiecki*, 2010; fig.S8].

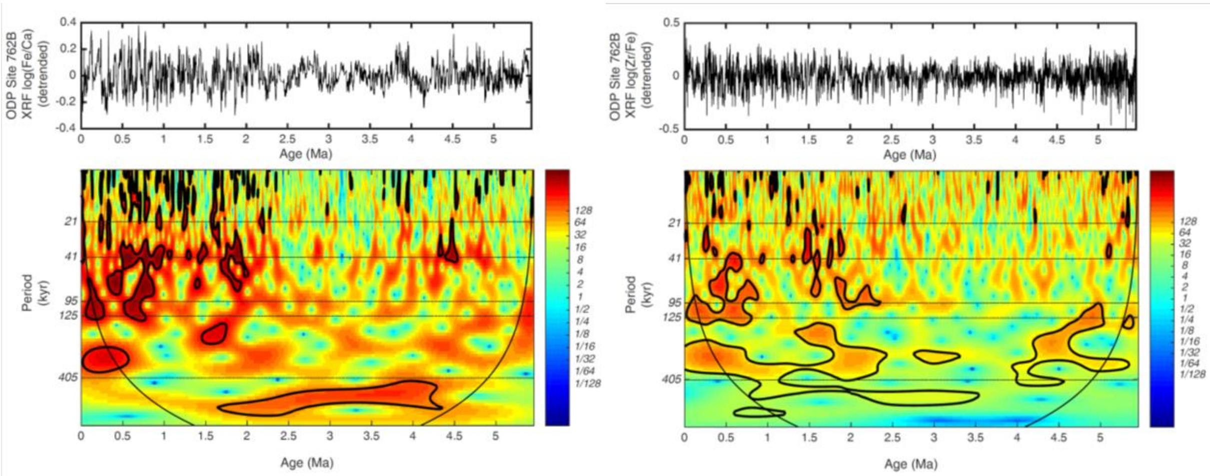

Figure S8. Power spectra of the XRF records Log(Fe/Ca) and Log(Zr/Fe for core ODP122-762B). See text above for more information.

Cited references

Anthonissen, D. E., and J. G. Ogg (2012), Appendix 3 - Cenozoic and Cretaceous Biochronology of Planktonic Foraminifera and Calcareous Nannofossils, in *The Geologic Time Scale*, edited, pp. 1083-1127, Elsevier, Boston.

Dare, R. A. (2013), Seasonal Tropical Cyclone Rain Volumes over Australia, *Journal of Climate*, *26*(16), 5958-5964.

Dare, R. A., N. E. Davidson, and J. L. McBride (2012), Tropical Cyclone Contribution to Rainfall over Australia, *Monthly Weather Review*, *140*(11), 3606-3619.

Ducassou, E., T. Mulder, S. Migeon, E. Gonthier, A. Murat, M. Revel, L. Capotondi, S. M. Bernasconi, J. Mascle, and S. Zaragosi (2008), Nile floods recorded in deep Mediterranean sediments, *Quaternary Research*, *70*(3), 382-391.

Grinsted, A., J. C. Moore, and S. Jevrejeva (2004), Application of the cross wavelet transform and wavelet coherence to geophysical time series, *Nonlinear Processes in Geophysics*, *11*, 561-566.

Haq, B. U., et al. (1990), Site 762, *Affiliation (analytic): Natl. Sci. Found., Mar. Geol. and Geophys., Washington, DC*, *122*, 213.

Hopkins, J., M. Lucas, C. Dufau, M. Sutton, J. Stum, O. Lauret, and C. Channelliere (2013), Detection and variability of the Congo River plume from satellite derived sea surface temperature, salinity, ocean colour and sea level, *Remote Sensing of Environment*, *139*, 365-385.

Kang, Y., D. Pan, Y. Bai, X. He, X. Chen, C.-T. A. Chen, and D. Wang (2013), Areas of the global major river plumes, *Acta Oceanologica Sinica*, *32*(1), 79-88.

Kuhnt, W., A. Holbourn, J. Xu, B. Opdyke, P. De Deckker, U. Röhl, and M. Mudelsee (2015), Southern Hemisphere control on Australian monsoon variability during the late deglaciation and Holocene, *Nature Communications*, *6*, 5916.

Lisiecki, L. E. (2010), Links between eccentricity forcing and the 100,000-year glacial cycle, *Nature Geoscience*, *3*(5), 349-352.

Lisiecki, L. E., and M. E. Raymo (2005), A Pliocene-Pleistocene stack of 57 globally distributed benthic δ^{18}O records, *Paleoceanography*, *20*(1), PA1003.

Liu, Y., X. S. Liang, and R. H. Weisberg (2007), Rectification of the Bias in the Wavelet Power Spectrum, *Journal of Atmospheric and Oceanic Technology*, *24*(12), 2093-2102.

Palma, E. D., and R. P. Matano (2017), An idealized study of near equatorial river plumes, *Journal of Geophysical Research: Oceans*, *122*(5), 3599-3620.

Prins, M. A., G. Postma, J. Cleveringa, A. Cramp, and N. H. Kenyon (2000), Controls on terrigenous sediment supply to the Arabian Sea during the late Quaternary: the Indus Fan, *Marine Geology*, *169*, 327-349.

Shanmugam, G. (2018), A global satellite survey of density plumes at river mouths and at other environments: Plume configurations, external controls, and implications for deep-water sedimentation, *Petroleum Exploration and Development*, *45*(4), 640-661.

Spooner, M. I., P. De Deckker, T. T. Barrows, and L. K. Fifield (2011), The behaviour of the Leeuwin Current offshore NW Australia during the last five glacial-interglacial cycles, *Global and Planetary Change*, *75*(1), 119-132.

Stuut, J.-B. W., and F. Lamy (2004), Climate variability at the southern boundaries of the Namib (southwestern Africa) and Atacama (northern Chile) coastal deserts during the last 120,000 yr, *Quaternary Research*, *62*(3), 301-309.

Stuut, J.-B. W., F. Temmesfeld, and P. De Deckker (2014), A 550 kyr record of aeolian activity near North West Cape, Australia: inferences from grain-size distributions and bulk chemistry of SE Indian Ocean deep-sea sediments, *Quaternary Science Reviews*, *83*, 83-94.

Stuut, J.-B. W., S. Kasten, F. Lamy, and D. Hebbeln (2007), Sources and modes of terrigenous sediment input to the Chilean continental slope, *Quaternary International*, *161*, 67-76.

Stuut, J.-B. W., M. A. Prins, R. R. Schneider, G. J. Weltje, J. H. F. Jansen, and G. Postma (2002), A 300-kyr record of aridity and wind strength in southwestern Africa: inferences from grain-size distributions of sediments on Walvis Ridge, SE Atlantic, *Marine Geology*, *180*(1-4), 221-233.

Tang, C. (1992), Paleomagnetism of Cenozoic sediments in Holes 762B and 763A, central Exmouth Plateau, Northwest Australia., in *Proceedings of the Ocean Drilling Program, Scientific Results*, edited by U. Von Rad, B. U. Haq and et al, pp. 717-733, Ocean Drilling Program, College Station, TX.

Torrence, C., and G. P. Compo (1998), A Practical Guide to Wavelet Analysis, *Bulletin of the American Meteorological Society*, *79*(1), 61-78.

Wells, P. E., and A. R. Chivas (1994), Quaternary foraminiferal bio- and isotope stratigraphy of ODP Holes 122–760A and 122–762B, Exmouth and Wombat Plateaus, northwest Australia, *Australian Journal of Earth Sciences*, *41*(5), 455-462.

Weltje, G. J., and R. Tjallingii (2008), Calibration of XRF core scanners for quantitative geochemical logging of sediment cores: Theory and application, *Earth and Planetary Science Letters*, *274*(3–4), 423-438.